J. Fluid Mech. (2008), *vol.* 611, *pp.* 237–254.
doi:10.1017/S0022112008002796 Printed in the United Kingdom

Exchange flow between a canopy and open water

MIRMOSADEGH JAMALI[1], XUEYAN ZHANG[2] AND HEIDI M. NEPF[2]

[1]Department of Civil Engineering, Sharif University of Technology, Azadi Avenue, Teheran, Iran

[2]Department of Civil and Environmental Engineering, Massachusetts Institute of Technology, Cambridge, Massachusetts, USA

(Received 24 September 2007 and in revised form 30 May 2008)

This paper theoretically and experimentally investigates the exchange flow due to temperature differences between open water and a canopy of aquatic plants. A numerical model is used to study the interfacial shape, frontal velocity and total volumetric exchange, and their dependence on a dimensionless vegetation drag parameter. The numerical predictions are consistent with the laboratory measurements. There is a short initial period in which the force balance is between buoyancy and inertia, followed by drag-dominated flow for which there is a balance between buoyancy and drag forces. After the initial stage, the gravity current propagating into the canopy takes a triangular shape whereas the current propagating into the open water has almost the classic unobstructed horizontal profile, but with a slowly decreasing depth. Near the edge of the canopy, but in the open region, the flow is found to be critical with a unit internal Froude number. The exchange flow rate and the front speed in the canopy decrease slowly with time whereas the gravity current in the open water has a constant speed. The magnitude of the exchange flow decreases as the canopy drag increases. Empirical equations for the flow properties are presented. A movie is available with the online version of the paper.

1. Introduction

Spatial heterogeneity in water temperature, and thus density, can drive horizontal flow that carries fluxes between chemically distinct regions of a surface water body. These buoyancy-driven exchanges link the littoral and pelagic regions and play an important role in setting lake-scale chemistry (MacIntyre & Melack 1995; James & Barko 1991*a, b*, James, Barko & Eakin 1994). The spatial gradients in temperature may arise from differences in water depth, light penetration, and/or wind sheltering. Depth-driven differential heating and cooling has been observed to generate significant flow between littoral regions and the main body of a lake, with observed velocities as high as $15\,\mathrm{cm\,s^{-1}}$ (Roget & Colomer 1996; Monismith, Imberger & Morison 1990; Adams & Wells 1984). These flows have been studied extensively through both physical experiment (Sturman & Ivey 1998; Sturman, Oldham & Ivey 1999; Lei & Patterson 2002), and numerical modelling (Farrow & Patterson 1993, 1994; Horsch, Stefan & Gavali 1994; Lei & Patterson 2003). Flows of somewhat smaller magnitude, 1 to $3\,\mathrm{cm\,s^{-1}}$, can arise from spatial gradients in water clarity (e.g. Nepf & Oldham 1997; MacIntyre, Romero & Kling 2002).

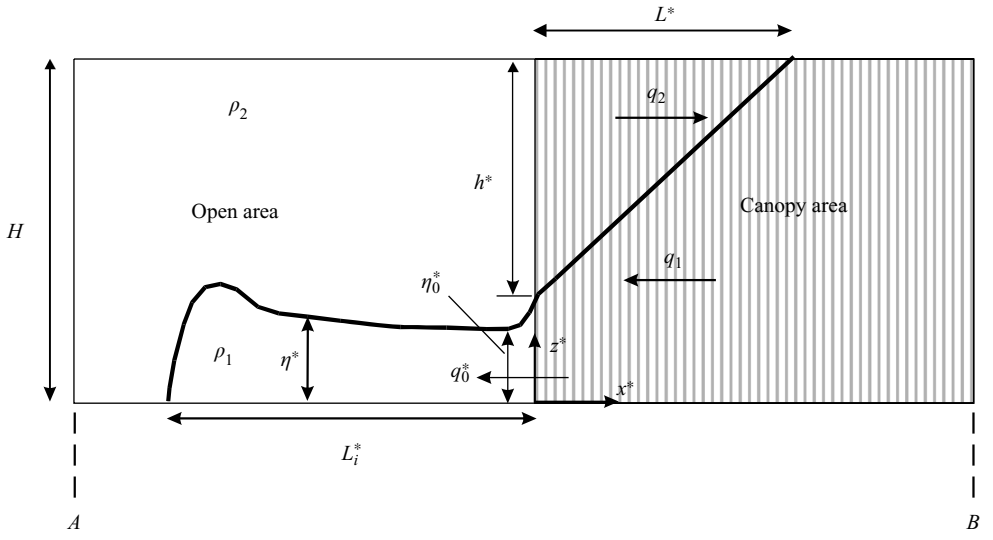

FIGURE 1. Definition of parameters in lock-exchange flow between open water and canopy.

Emergent vegetation is a common feature in the littoral region, yet only a handful of studies have considered its impact on buoyancy-driven exchange. Because vegetation produces a significant additional drag, it should reduce the magnitude of the currents. Oldham & Sturman (2001), who parameterized vegetative drag using permeability, predicted and observed a reduction in steady, buoyancy-driven, down-slope flow in both the laboratory and field. Tanino, Nepf & Kulis (2005) applied quadratic and linear drag laws to describe exchange flows occurring entirely within the canopy. They showed that for sparse vegetation the flow has the same interfacial shape as a classic gravity current, but is diminished in magnitude. For dense vegetation, the interface becomes linear.

In addition to providing drag, vegetation can also contribute to differential heating. Water temperature gradients can be generated by mats of floating vegetation (Bowmaker 1976; Dale & Gillespie 1976) and by scum layers (Zohary & Madeira 1990), because the water beneath the opaque layer heats more slowly than adjacent uncovered water. Coates & Patterson (1993, 1994) described the resulting fluid exchange, but only considered the flow beneath the floating root layer, and thus neglected the vegetative drag. Emergent plants also provide shading that can damp the daily heating cycle, resulting in temperature differences of up to 3° C between an emergent canopy and adjacent open water (e.g. Ultsch 1973; Sartoris *et al.* 2000; Chimney, Wenkert & Pietro 2006). Unlike the floating mats studied by Coates & Patterson (1993, 1994), the drag contributed by emergent plants cannot be neglected, as it is distributed over the entire flow domain.

In this paper we consider the role of canopy drag in controlling the exchange between an emergent canopy and adjacent open water. The problem is simplified as a lock-exchange flow driven by a constant density difference between a canopy area and the adjacent open water (figure 1), and is studied both numerically and experimentally. The paper is structured as follows. The numerical model and the laboratory experiments are discussed in § 2 and § 3, respectively. The results are discussed in § 4. Finally, concluding remarks are given in § 5.

2. Numerical model

The lock-exchange problem has been widely used as a simple model to study exchange flows. Here, the flow domain is modified by placing a canopy into one of the initial reservoirs. The canopy is modelled as an array of circular cylinders having diameter d and frontal area per unit volume a. The porosity n (the volume fraction occupied by water) is given by $1-(\pi/4)ad$. In general, n can be a function of x and z. A schematic is shown in figure 1. The system is two-dimensional with a total water depth H. The origin of the dimensional coordinate system x^*–z^* is located at the lock, which is at the mid-length of the tank. The time is denoted by t^*, the velocity vector $\boldsymbol{V}^*$ by (u^*, w^*), the general density by ρ^*, the interface height above the bed by η^* and the depth of the upper layer at the origin by h^*. In the open area, η^* becomes the height of the gravity current; ρ_1 and ρ_2 are the densities of the heavy and light fluids, respectively. The fluid is assumed to be incompressible and viscous.

The characteristic time scale is N^{-1}, where the frequency $N=\sqrt{g'/H}$ and $g'=g(\rho_1-\rho_2)/\rho_1$ is the reduced gravitational acceleration. Taking H to be the characteristic length scale, $U=NH$ is the characteristic velocity scale. We normalize the physical variables as follows,

$$\left.\begin{array}{l}(x,z)=(x^*/H, z^*/H),\ t=t^*N,\ (u,w)=(u^*/U, w^*/U),\\ \eta=\eta^*/H,\ \gamma=(\rho^*-\rho_1)/(\rho_1-\rho_2),\end{array}\right\} \tag{1}$$

where (x, z) and t are dimensionless independent variables, and (u, w), η and γ are dimensionless dependent variables. In general, time, length, and velocity are normalized with N^{-1}, H and U, respectively. Throughout this paper, the dimensionless form of a parameter having an asterisk is shown without the asterisk.

The canopy drag is described by a quadratic drag law, as in Tanino *et al.* (2005). Assuming a is homogeneous and isotropic, the canopy drag force per volume is $0.5\rho^* C_D a V^{*2}$, in which C_D is the canopy drag coefficient. Note that this formulation assumes a spatial average over a scale greater than several stems, such that the drag associated with discrete stems is represented as a bulk resistance. In general, the drag coefficient C_D is a function of the cylinder Reynolds number $Re_d=V^*d/\nu$ with ν being the kinematic viscosity, and the canopy porosity n (e.g. as discussed in Tanino and Nepf, 2008). For canopies with high porosity, the canopy drag coefficient matches that for an isolated circular cylinder, i.e. for $1<Re_d<10^5$, C_D is given by the empirical expression

$$C_D=1+10Re_d^{-2/3} \tag{2}$$

(White 1991, p. 183). For the range of $Re_d<700$, which is relevant in the current study, C_D increases with decreasing porosity, for porosity less than 95%. This increase reflects the enhanced viscous stress associated with the smaller cylinder spacing, see Tanino & Nepf (2008). This trend is born out in the calibration of the numerical model and is discussed below.

Incompressibility requires

$$\frac{\partial\gamma}{\partial t}+u\frac{\partial\gamma}{\partial x}+w\frac{\partial\gamma}{\partial z}=0. \tag{3}$$

Using the Boussinesq approximation, i.e. $(\rho_1-\rho_2)/\rho_1\ll 1$, and ignoring the friction from the walls and bottom of the tank, the momentum equations can be written as

$$\frac{\partial u}{\partial t}+u\frac{\partial u}{\partial x}+w\frac{\partial u}{\partial z}=-\frac{\partial P}{\partial x}+Re^{-1}\nabla^2(u)-\frac{1}{2}\frac{C_D a H}{n}Vu, \tag{4a}$$

$$\frac{\partial w}{\partial t} + u\frac{\partial w}{\partial x} + w\frac{\partial w}{\partial z} = -\frac{\partial P}{\partial z} + Re^{-1}\nabla^2(w) - \frac{1}{2}\frac{C_D a H}{n} V w - \gamma, \tag{4b}$$

where $P = (P^* - \rho_1 g z)/\rho_1 U^2$ is the dimensionless dynamic pressure with P^* being the total pressure, $Re = UH/\nu$, and $\nabla^2 = \partial^2/\partial x^2 + \partial^2/\partial z^2$. The array drag terms are similar to those in Tanino *et al.* (2005). Note that the above formulation assumes that the frontal area per volume is isotropic, such that the canopy drag forces for the x- and z-components of the flow have the same form. This may not fully represent a vegetated area. For many canopies, a is anisotropic, and hence $C_D a$ for the z-component is different from that for the x-component, as the orientation of the flow relative to the cylinder or reed stem is different. However, since the flow is generally horizontal, the solution is not very sensitive to the description of the vertical drag component.

Finally, continuity requires

$$\frac{\partial (nu)}{\partial x} + \frac{\partial (nw)}{\partial z} = 0. \tag{5}$$

By combining the momentum equations and approximating the viscosity and the drag terms by $Re^{-1}\nabla^2\zeta$, the vorticity equation is obtained as

$$\frac{\partial \zeta}{\partial t} + u\frac{\partial \zeta}{\partial x} + w\frac{\partial \zeta}{\partial z} = \frac{\partial \gamma}{\partial x} - \frac{1}{2}\bar{C}\left(\frac{\partial (Vu)}{\partial x} - \frac{\partial (Vw)}{\partial x}\right) + Re^{-1}\nabla^2\zeta + \frac{u}{n}\frac{\partial n}{\partial x}\zeta + \frac{w}{n}\frac{\partial n}{\partial z}\zeta \tag{6}$$

where vorticity $\zeta = \partial u/\partial z - \partial w/\partial x$, and we define the new dimensionless canopy drag parameter $\bar{C} = C_D a H/n$. From the continuity equation, $u = n^{-1}\partial\Psi/\partial z$ and $w = -n^{-1}\partial\Psi/\partial x$, in which Ψ is a stream function. As a result,

$$\zeta = \frac{1}{n}\nabla^2\Psi + \frac{\partial}{\partial z}\left(\frac{1}{n}\right)\frac{\partial \Psi}{\partial z} + \frac{\partial}{\partial x}\left(\frac{1}{n}\right)\frac{\partial \Psi}{\partial x}. \tag{7}$$

Equations (3), (6) and (7) are subject to the initial conditions $\zeta = \Psi = 0$ everywhere, $\gamma = 0$ for $x > 0$, and $\gamma = -1$ for $x < 0$. The boundary conditions are $\Psi = u = 0$ at the bed, and $\Psi = \zeta = 0$ at $z = 1$ and the side walls. The zero vorticity boundary condition corresponds to a slip flow.

Three dimensionless parameters $\bar{C}$, n and Re appear in the governing equations. In the field and laboratory the canopy drag typically dominates the viscous drag, so that the flow is only weakly dependent on Reynolds number Re. The typical range for ad in freshwater canopies is 0.01 to 0.1 corresponding to $n = 0.99$ to 0.92, respectively (Kadlec 1990; Kalff 2002), although n as low as 0.55 with mean trunk diameters in the range $d = 4$ to 9 cm have been reported in mangroves (Mazda *et al.* 1997; Furukawa, Wolanski & Mueller 1997). When n is close to unity, as in many real situations, $\bar{C}$ alone parameterizes the flow. Specifically, since $\bar{C}$ is only a weak function of g' through $C_D = f(Re_d)$, the exchange flows in a particular canopy (fixed $\bar{C}$) will be nearly identical in dimensionless space, regardless of the density difference represented by g'. This will be verified experimentally later. In most marshes, the stem diameter is in the range $d = 0.2$ to 1.2 cm; the flow depth is typically between 10 and 100 cm; the canopy porosity $n > 0.92$ and the local flow speed is in the range 1 to 10 cm s^{-1} (e.g. Valiela, Teal & Deuser 1978; Leonard & Luther 1995). These conditions suggest that the dimensionless canopy drag $\bar{C}$will typically be in the range 1 to 30 in the field.

The equations of motion are solved using a finite-difference technique. The domain is discretized uniformly in the x- and z-directions. To minimize numerical diffusion

associated with the discretization, the ULTIMATE QUICKEST scheme (Leonard 1991) is used to approximate equation (3). The left-hand side of (6) is discretized using an explicit upwind scheme (first-order accurate in time and space). The terms on the right-hand side of (6) are approximated by a central scheme (second-order accurate). Equation (3) is solved at all the grid points, while equation (6) is solved at the interior grid points, and the boundary conditions for velocity and ζ are applied to the remaining grid points. Equation (7) is elliptic and is solved using the standard over-relaxation scheme. A central three-point scheme is used to discretize the equation at the interior points. The boundary conditions for Ψ are used for the boundary points. The process of the flow calculation is as follows. First, γ and ζ at the next time step $(m+1)$ for all the grid points are obtained from discretization of (3) and (6), respectively. Having ζ^{m+1}, equation (7) is then solved for Ψ^{m+1} for the interior grid points using an over-relaxation parameter of 1.8.

The flow was simulated for a range of $\bar{C}$ between 0.01 and 150 for the canopy porosity $n = 0.98$ in a numerical tank of length 20 using 320 grid spacings in the x-direction and 80 in the z-direction with $\Delta t = 0.004$ and $Re = 10^6$. As the stem drag typically dominates the viscous drag, the simulations are not very sensitive to the value of Re. For simulations of the experimental conditions, 160 grid spacings in the x-direction and 80 in the z-direction with $\Delta t = 0.002$ were used. Convergence tests confirmed the accuracy of the results.

Model calibration is necessary before carrying out the numerical simulations. The full-canopy experiments 17, 36, and 42 reported in Tanino *et al.* (2005) were used to calibrate the expression for the drag coefficient. The calibration indicated that the coefficient 10 in equation (2) should be increased to 50 to achieve a close match between the experimental and the numerical interface displacement (as shown in figure 2). This increase in drag coefficient is consistent with trends noted in Tanino & Nepf (2008), i.e. drag coefficients increased, relative to the isolated cylinder, for $Re_d < 700$, consistent with the conditions considered here. It is seen that both the shape of the interface and the positions of the fronts have been matched by the numerical model. Hence, the expression

$$C_D = 1 + 50Re_d^{-2/3} \tag{8}$$

will be used for all simulations to follow, with no additional fitting or calibration. Note that the velocity varies throughout the domain, as does C_D.

3. Experiments

A set of laboratory experiments was conducted to provide validation data for the half-canopy configuration. The experiments were conducted in a $120\,\text{cm} \times 12.0\,\text{cm} \times 20.0\,\text{cm}$ Plexiglas tank separated into two reservoirs of equal length by a removable gate which was 5 mm thick. A model canopy was placed in the right-hand side of the tank. The model consisted of 6 mm circular cylinders held in place by a perforated board. The board was supported by the tank walls, and the cylinders were inserted from the top and reached down to the tank bed. The holes of the perforated board were drilled at random locations. Each of the holes was assigned a number and a numerical program was used to randomly select a subset of holes for filling. Three experiments were run at a solid volume fraction of approximately 6%, which corresponds to $a = 0.14\,\text{cm}^{-1}$ and $n = 0.94$. For each experiment the reservoir containing the model canopy was filled with saltwater coloured with food dye for visualization. The open region was filled with fresh water. The density of water in

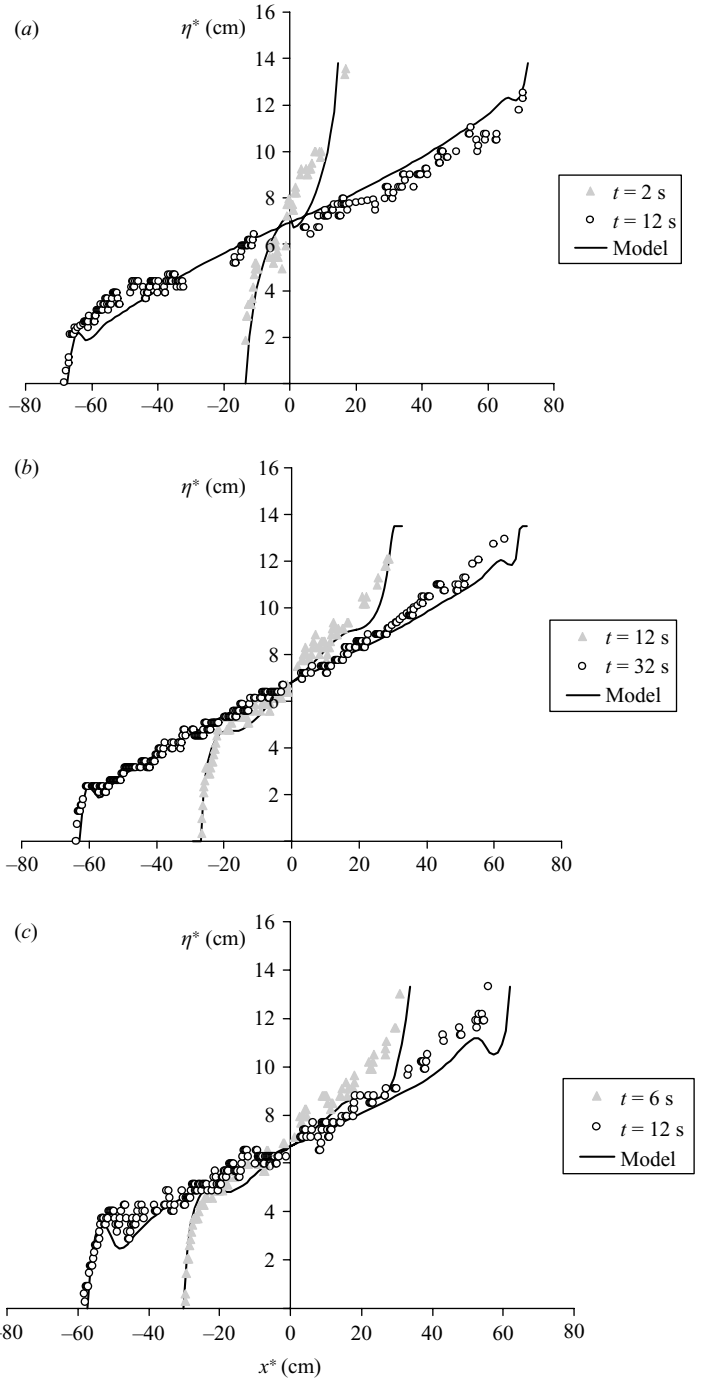

FIGURE 2. Comparison of the measured interface profiles with the predictions of the numerical model for (*a*) experiment 17 ($a = 0.12\,\mathrm{cm}^{-1}$, $g' = 33.8\,\mathrm{cm\,s}^{-2}$, $H = 13.8\,\mathrm{cm}$), (*b*) experiment 36 ($a = 0.068\,\mathrm{cm}^{-1}$, $g' = 4\,\mathrm{cm\,s}^{-2}$, $H = 13.5\,\mathrm{cm}$), and (*c*) experiment 42 ($a = 0.068\,\mathrm{cm}^{-1}$, $g' = 18.1\,\mathrm{cms}^{-2}$, $H = 13.3\,\mathrm{cm}$) of Tanino *et al.* (2005). $d = 0.64\,\mathrm{cm}$ in the experiments.

Run	d (cm)	a (cm^{-1})	Canopy porosity	H (cm)	g' (cm s^{-2})	C_D (Eq. (8))	$\bar{C}$
A	0.6	0.14	0.93	11.0	11.9	2.3	3.8
B	0.6	0.14	0.93	11.2	9.25	2.4	4.1
C	0.6	0.13	0.94	11.5	8.30	2.5	4.0
D	0.6	0.11	0.95	10.0	9.24	2.5	2.8
E	0.6	0.085	0.96	10.6	4.89	2.9	2.7

TABLE 1. Experimental parameters for the validation runs.

each region was measured with a hydrometer with a precision of 0.0005 g cm^{-3}. The experimental parameters for each run are given in table 1.

The tank was backlit with 40 W fluorescent tube lights. The light was diffused by sheets of tracing paper attached to the back of the tank. The evolution of the interface was tracked using a 640×480 CCD camera at a rate of 1 f.p.s. The camera was mounted on a tripod located 5.4 m from the front of the tank, which was sufficiently far from the tank to reduce parallax error to less than 1%. Matlab's image processing module was used to locate the interface location η^* by standard edge detection techniques. The velocity within the canopy model was estimated by tracking the position of the toe within the canopy, which is defined as the x -position at which $\eta^* = H$. The toe velocity averaged over the duration of the experiment may be used to estimate $C_D = f(Re_d)$ from equation (8). The computed C_D is given in table 1 along with the corresponding $\bar{C}$.

4. Results

Contours of constant density, predicted numerically, reveal the evolution of the exchange flow under the Run C conditions (figure 3). The experimentally measured interface position for this case is plotted as circles. In the numerical model, local fluid velocity was used to calculate C_D from equation (8). A reasonable agreement between the experiment and the model is observed. In particular, the progression of the toe within both the open region and the canopy is captured by the numerical model. In addition, the distinct interfacial shapes within the two regions are reproduced by the numerical model. The interface is triangular within the canopy, but nearly horizontal in the open region. This comparison validates the model and the use of the calibrated equation (8) for the drag coefficient. The difference between the modelled and the measured interface may be due to differences in the initial condition and to measurement errors. In the laboratory experiment, the action of lifting the gate creates local vorticity and some mixing. This does not occur in the numerical experiment, in which the gate disappears without creating any fluid motion.

As discussed previously, the dimensionless form of the exchange flow is dependent on the canopy drag, but it is almost independent of the density difference. To show this, the interface profiles in two experiments (D and E) in the same canopy but with different density differences (g') are plotted in figure 4. These profiles correspond to almost the same dimensionless drag parameter ($\bar{C} \approx 2.7$) at dimensionless times $t = 8.7$ and 19.5. After normalization, the two profiles for the different density cases collapse, indicating that the behaviour of the exchange flow is independent of the density difference.

Development of the flow in a numerical tank for $\bar{C} = 13.2$ is shown in figure 5; see the corresponding animation available with the online version of the paper. Just after

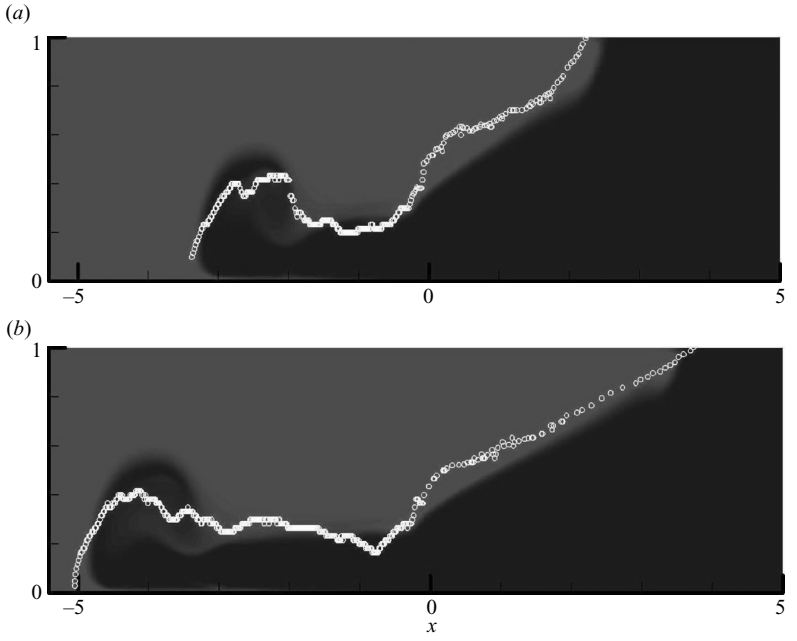

FIGURE 3. Development of the exchange flow in experiment C (white circles) in dimensionless form and comparison with the results of the numerical model. (*a*) $t^* = 10\,\mathrm{s}$ ($t = 8.5$), (*b*) $t^* = 15\,\mathrm{s}$ ($t = 12.8$).

the gate is released, the flow in both open and canopy areas is dominated by inertia as indicated by the shape of the interface. The interface pivots close to mid-depth ($z = 0.5$), just as in an energy-conserving current ($t = 0.6$). As the front enters the canopy a greater volume of fluid is affected by drag, and eventually the drag forces dominate over inertia, as shown by the following progression (see also figure 5). The numerical results show that the array drag term in (4) is much smaller than the inertia terms for $t < 0.4$. The drag term increases in magnitude with time, and around $t = 0.8$ it is comparable to the inertia terms. At $t = 6$ the stem drag term becomes about 10 times as large as the inertia terms. This ratio increases to 20 at $t = 14$. However, since the interface has a memory of its initial development, the profile in the canopy is not fully linear until a much later time.

Once the drag-dominated regime is reached, the front speed in the canopy area begins to decline with time, which was predicted and observed by Tanino *et al.* (2005) for a lock-exchange within a full canopy. However, the flow in the open area continues to resemble a free gravity current, with the front moving at a constant speed. Note also that there is no flow in the regions beyond the two fronts (e.g. examine the velocity field at $t = 8$, figure 5). The constant propagation of the open-water front is further demonstrated in figure 6, which presents the modelled and observed position of the toe within the open region, L_i^*, at different times in experiments A, B, and C. Both the model and the measurements indicate that the front has a constant speed. On the other hand, like the full canopy case, the less dense front moving on the surface into the canopy slows as it extends further into the canopy. This is shown in figure 7, which gives the numerical results for the temporal evolution of the dimensionless toe position L in the canopy area for $\bar{C} = 13.2$.

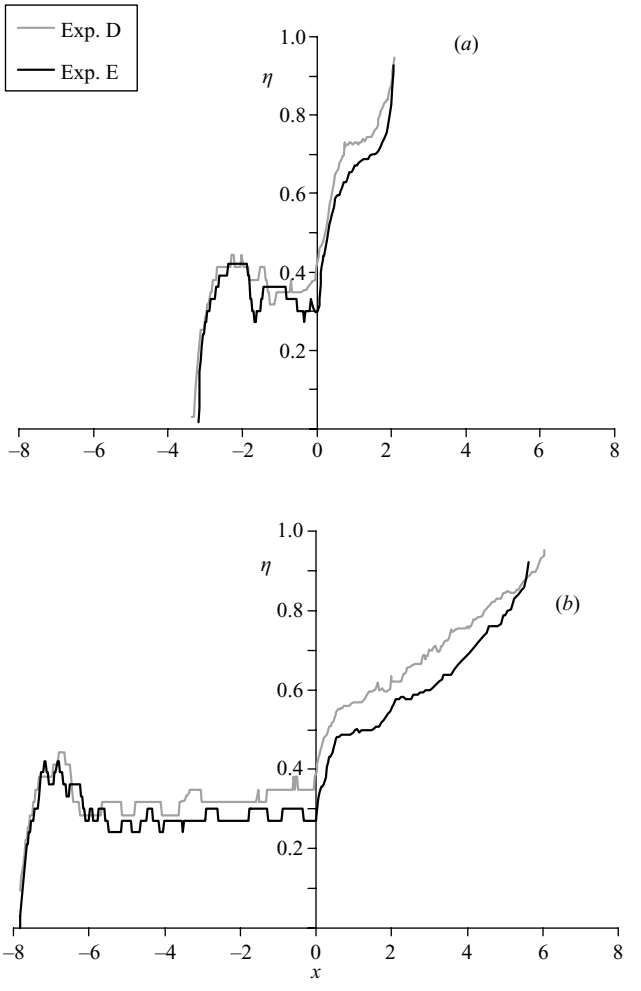

FIGURE 4. Comparison of the interface profiles in experiment D ($\bar{C} = 2.8$) and E ($\bar{C} = 2.7$) at (*a*) $t = 8.7$ and (*b*) $t = 19.5$.

An interesting feature of the half-canopy exchange flow is that the interface becomes horizontal in the open region at a point very close to the junction with the canopy (see figure 5, $t = 12$). This point represents a critical point in the sense that the internal Froude number in the lower layer is unity. The dimensionless flow depth and the flow rate per unit width at this point are denoted by η_0 and q_0, respectively, see figure 1. The Froude number is defined as the fluid velocity in the lower layer q_0/η_0 over the long internal wave speed $\sqrt{\eta_0(1-\eta_0)}$. In general, q_0 may be taken as the flow rate at the origin as the critical point is close to the canopy. From the condition of Froude number equal to one, we anticipate that the volumetric flux at the critical point is $q_0 = \sqrt{\eta_0^3(1-\eta_0)}$. This can be demonstrated using data taken from Zhang & Nepf's (2008) experimental study. Figure 8 compares the experimentally measured q_0 as a function of η_0 with the relation $q_0 = \sqrt{\eta_0^3(1-\eta_0)}$. The agreement between the experiments and the equation supports the hypothesis of a critical flow close to the junction.

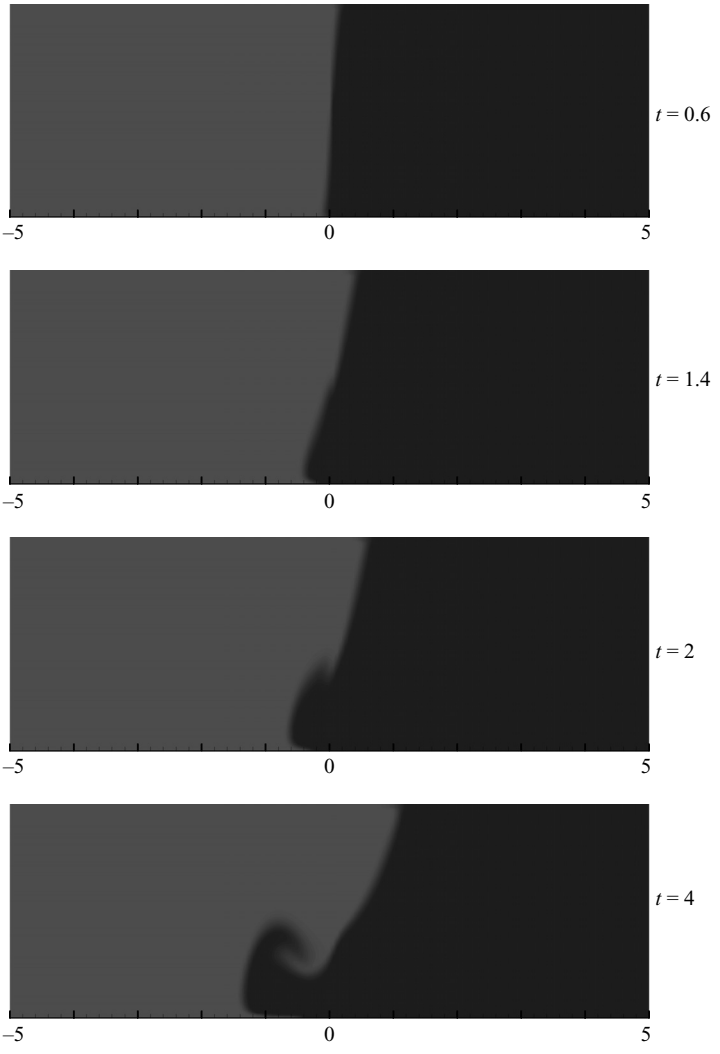

FIGURE 5. For caption see facing page.

The numerical experiments provide a vehicle for exploring the variation of q_0, η_0 and toe velocity with time, as well as understanding their dependence on the dimensionless drag parameter $\bar{C}$. First, consider the time evolutions of the dimensionless flow rate q_0 and dimensionless critical depth η_0, which are shown in figure 9(*a–c*) for $\bar{C} = 0.66$, 1.32 and 13.2. For simplicity, $\bar{C}$ was set constant throughout the domain for these runs. The critical depth is not plotted for t less than about 8 due to uncertainty in calculation of η_0 from the numerical results. For large times, the flow rate and critical depth decrease so slowly with time that they can be considered to have reached a quasi-steady condition in a normalized time of order 10. The area below the curve $q_0(t)$ represents the volume of fluid exchanged between the canopy and open area since $t = 0$, which is seen to increase with time. The time variation of q_0 predicted by the critical depth assumption, i.e. $q_0 = \sqrt{\eta_0^3(1 - \eta_0)}$, is shown as a dashed line in figure 9. The modelled and predicted flow rates are nearly equal in all three cases, which again supports the existence of a critical depth.

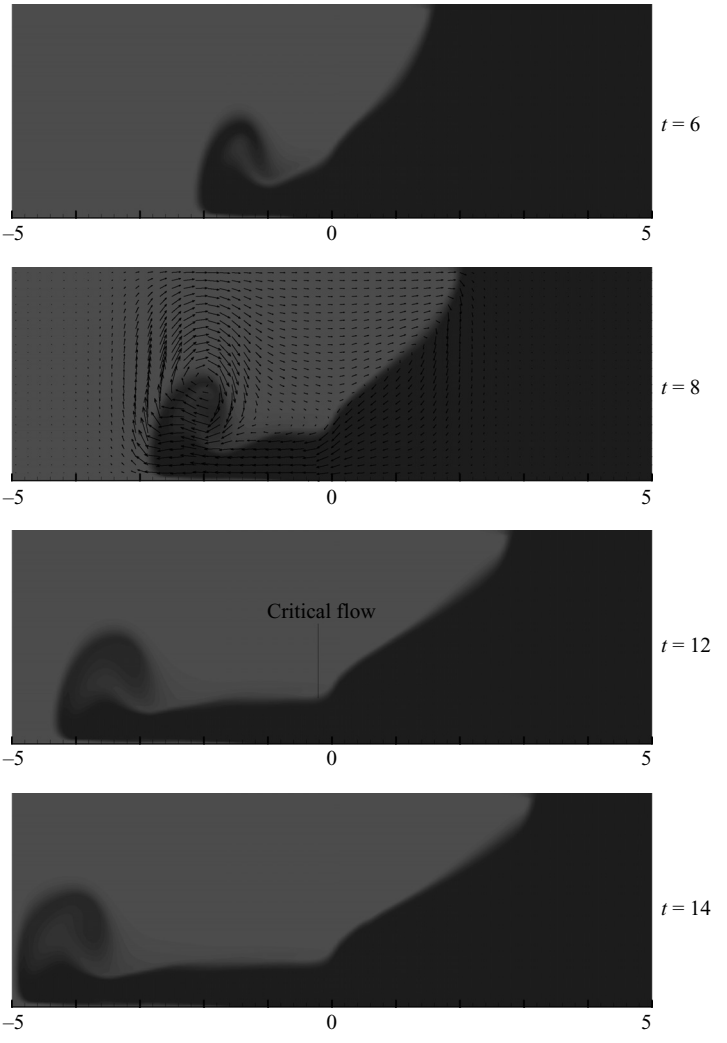

FIGURE 5. Development of the exchange flow in the half-canopy according to the numerical model for $\bar{C} = 13.2$; see the corresponding animation available with the online version of the paper.

To evaluate the dependence of discharge rate (q_0), critical depth (η_0) and toe velocity in the open area ($u_{toe,o}$) on dimensionless drag coefficient $\bar{C}$, we restrict our attention to the slowly varying conditions achieved after the initial transient condition, i.e. $t > 10$. The values of q_0, η_0, and $u_{toe,o}$ taken from the numerical simulations at $t = 14$ for different drag coefficients are shown as solid circles in figures 10(*a*), 10(*b*), and 10(*c*), respectively. Experimental observations from Zhang & Nepf (2008) are included for comparison and shown as open circles. A good agreement is observed between the numerical and experimental results. As expected, the flow rate, critical depth, and toe velocity decrease as dimensionless drag increases. For small drag coefficients, say $\bar{C} < 0.1$, the numerical data tend to approach the classic lock-exchange flow. For example, for $\bar{C} = 0.01$, $q_0 = 0.225$ and $u_{toe,o} = 0.40$, which are close to $q_0 = 0.25$ and $u_{toe,o} = 0.5$ from the classic inviscid solution of lock-exchange flow and the experimental value of $u_{toe,o} = 0.44$ by Shin *et al.* (2004). The presence of a stationary

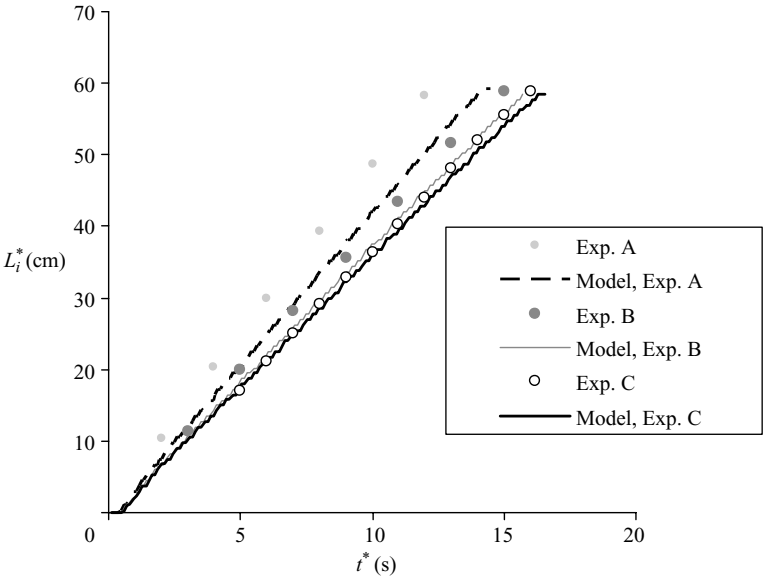

FIGURE 6. Comparison of the experimental and numerical results for the temporal evolution of the toe position in the open area.

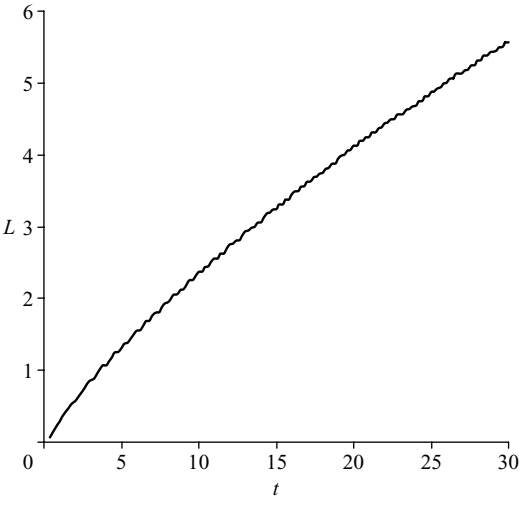

FIGURE 7. The temporal evolution of the dimensionless toe position in the canopy area taken from the numerical model for $\bar{C} = 13.2$.

vortex at $z = 0.5$ hindered accurate calculation of η_0 in the numerical simulation for $\bar{C} = 0.01$; however, a critical depth of close to 0.5 as suggested by the classic theory was indicated by the results.

The toe velocity in the open region, $u_{toe,o}$, is nearly constant and independent of the canopy drag for $\bar{C} < 3$ (figure 10*c*). This is explained by the fact that initially $\eta_0 = 0.5$, and from the kinematics of the interface motion the toe velocity is equal to the fluid velocity q_0/η_0 for small t. As such, from the critical flow condition $u_{toe,o} = \sqrt{\eta_0(1-\eta_0)} = 0.5$. For higher drag conditions, $\bar{C} > 3$, the current becomes thin enough for the viscous drag to reduce the toe speed.

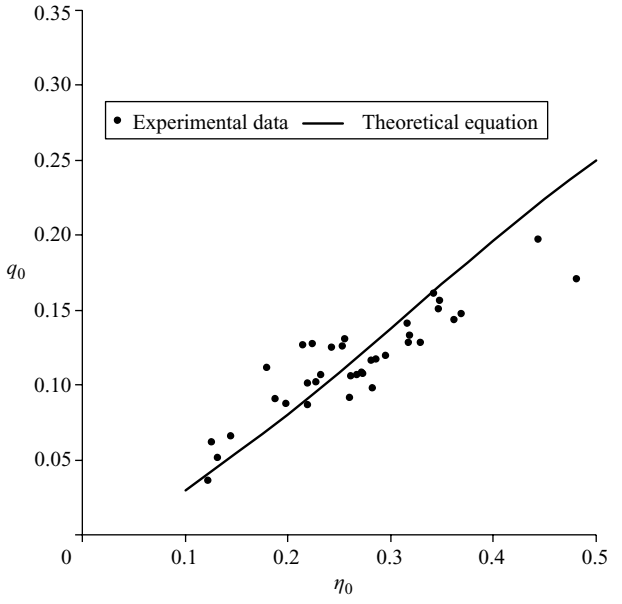

FIGURE 8. Plot of the experimental data for q_0 as a function of η_0 and comparison with the theoretical equation $q_0 = \sqrt{\eta_0^3(1-\eta_0)}$.

The equations of the best fits to the numerical data for $\bar{C} > 0.5$ are

$$q_0 = (0.15 \pm 12\%)\bar{C}^{(-0.30\pm16\%)}, \tag{9}$$

$$\eta_0 = (0.33 \pm 4\%)\bar{C}^{(-0.18\pm9\%)}. \tag{10}$$

The results of the numerical model for the dimensionless depth of the upper layer at the origin (h) at $t = 14$ for different $\bar{C}$ is given in figure 11. The equation of the best fit for $\bar{C} > 0.5$ is

$$h = (0.62 \pm 3\%)\bar{C}^{(0.043\pm28\%)}. \tag{11}$$

In general, $1 - h \neq \eta_0$. Defining $1 - h - \eta_0 \equiv \Delta$, Δ is given by

$$\Delta = (0.052 \pm 30\%)\bar{C}^{(0.16\pm74\%)}. \tag{12}$$

for $\bar{C} > 0.5$.

In the development of the above equations, $\bar{C}$ was assumed to be constant for a given configuration. On the other hand, Re_d is a function of both time and space owing to its dependence on local flow velocity, and so is $\bar{C}$. Practically, $\bar{C}$ may be approximated in advance by using the velocity scale $\sqrt{g'H}$ (a constant) in place of the local flow velocity in Re_d. This introduces only a small error in the estimate of the flow parameters. First, the two velocities are of the same order. Second, the flow parameters such as q_0 and η_0 are slow functions of $\bar{C}$, which means either definition of drag parameter gives almost the same values for the flow parameters.

It is also interesting to examine the reverse of the flow case that we have so far considered, i.e. having initially the less-dense water within the vegetation so that the less-dense gravity current flows into the open area at the surface and the dense gravity flow enters the canopy at the bottom. The numerical simulation for the reverse case is shown in figure 12 for $\bar{C} = 13.2$ at $t = 12$. Comparing the interface displacement at $t = 12$ in the original configuration (figure 5) shows that the free gravity flow has

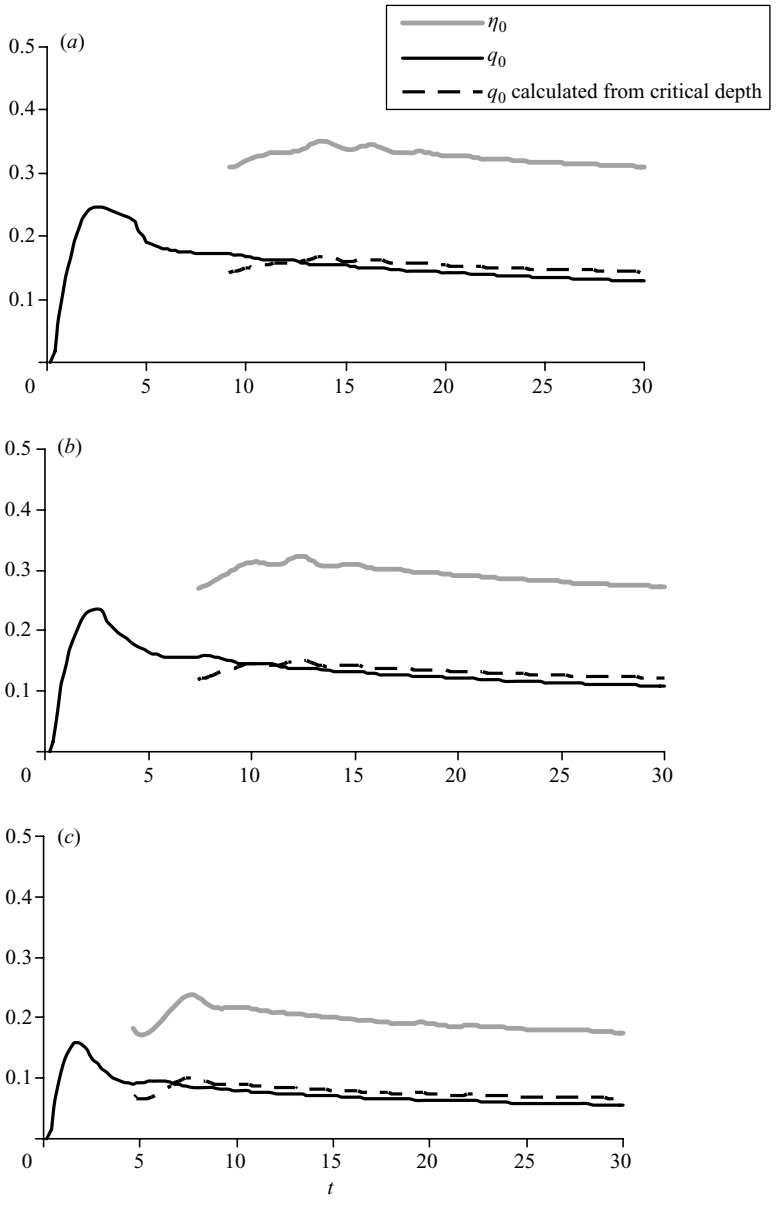

FIGURE 9. Temporal variation of q_0 and η_0 for (*a*) $\bar{C} = 0.66$, (*b*) $\bar{C} = 1.32$, and (*c*) $\bar{C} = 13.2$ according to the numerical model. Also plotted are calculated flow rates based on the assumption of the critical depth.

reached farther into the open area in the reverse case and is also thinner. However, the total volume intruded into the canopy and the front speed in the canopy is essentially the same. The front propagating into the open area has a greater speed in the reverse case, because it flows along a slip boundary (the free surface), in contrast to the original case in which it flows along the bed (a no-slip boundary). This shows that the frontal speed in the open region is affected by the condition of the boundary along which is travels, consistent with observations made for classic,

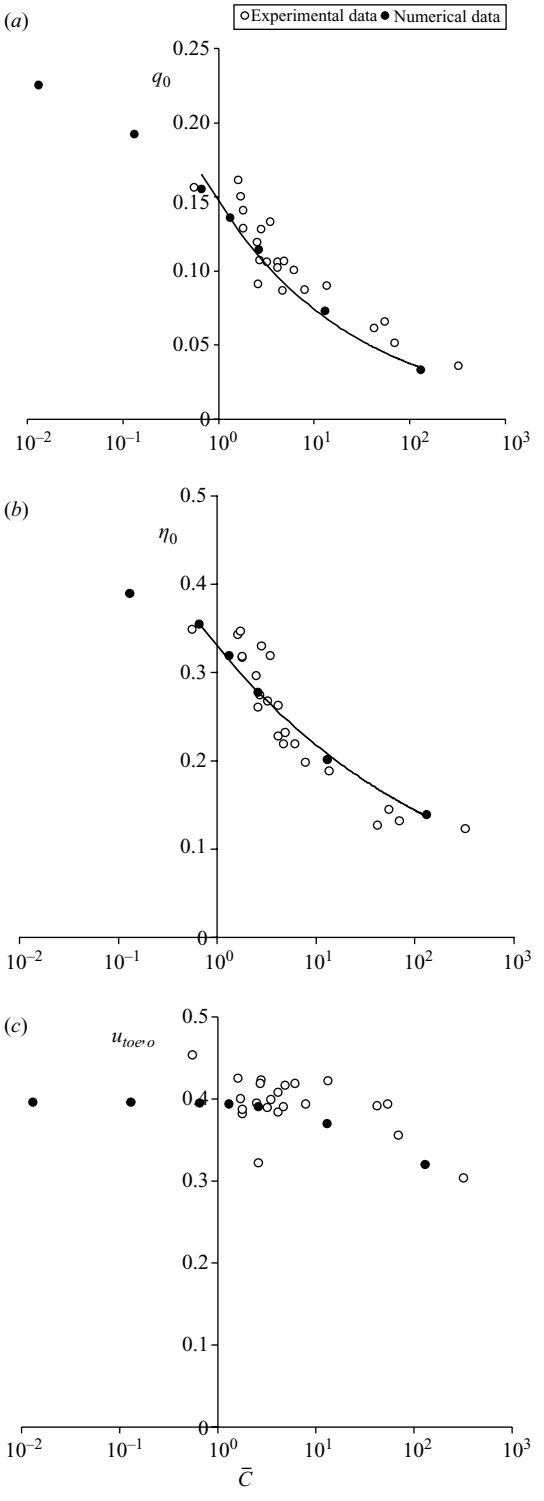

FIGURE 10. Comparison of the numerical and experimental data for (*a*) q_0, (*b*) η_0, (*c*) toe velocity in the open area as a function of $\bar{C}$. The numerical data correspond to $t = 14$.

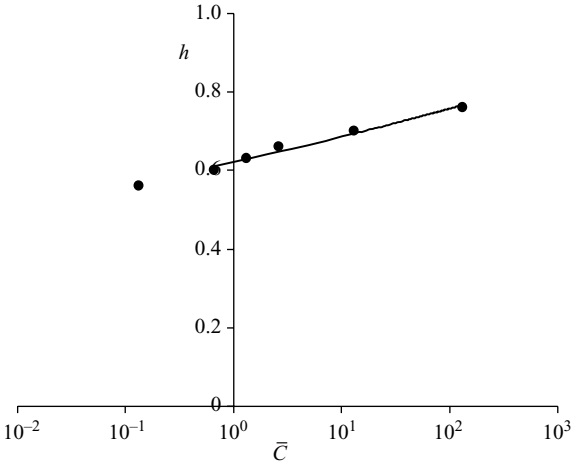

FIGURE 11. Variation of h (at $t = 14$) with $\bar{C}$ according to the numerical model.

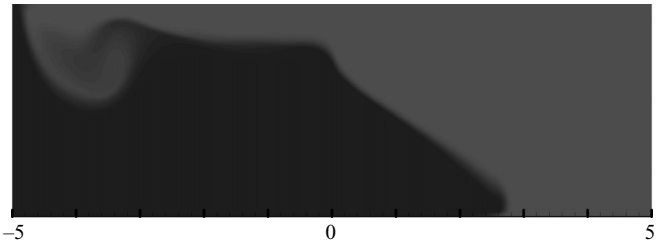

FIGURE 12. The exchange flow in the half-canopy when the canopy water is initially less dense than the open water; $t = 12$, $\bar{C} = 13.2$. The canopy is on the right-hand side.

unobstructed gravity currents. For example, in a classic lock-exchange Shin, Dalziel & Linden (2004) observed a higher toe velocity along the free surface than along the bed. Because the volumetric exchange is controlled by the canopy drag and virtually unchanged between the original and reversed cases, a higher frontal speed in the open region necessarily results in a thinner current in that region, simply by conservation of mass.

5. Concluding remarks

The exchange flow due to temperature differences between open water and a canopy of aquatic plants was investigated through numerical simulations and laboratory experiments. The problem was simplified as a lock-exchange flow. During the initial stage of the flow there is a force balance between buoyancy and inertia, and the flow in both canopy and open areas resemble the classic inviscid lock-exchange flow. After this initial, inertial phase, the fluid intruding into the canopy tends to a triangular shape. For large times, the force balance within the canopy shifts to a balance between buoyancy and vegetation drag. The density current in the open area moves with a constant nose speed and has the block shape of an unobstructed gravity current, but with a depth smaller than that in the inviscid lock-exchange flow. The magnitude of the exchange flow is a function of the drag parameter. Specifically, with a denser canopy and hence a larger drag parameter, the toe velocity within the canopy as well

as the total exchange flow rate decrease. For $\bar{C} > 3$, the toe velocity in the open region also decreases noticeably, because the depth of the gravity flow in the open area has also decreased.

The empirical equations can be used to give an estimate of the exchange flow in field situations. For a 3 K temperature difference between canopy and open water (see e.g. Sartoris *et al.* 2000; Chimney *et al.* 2006) in a water of depth of 1 m, the flow rate per unit width varies between 3×10^{-3} and $10 \times 10^{-3}\,\mathrm{m^2\,s^{-1}}$ for $\bar{C} = 1$ to 100, which is the range of the drag parameter in most real situations. Taking the effective daily flow duration to be 5 hours, the volume of fluid exchanged is between 50 to $170\,\mathrm{m^3\,m^{-1}}$. Thus, the exchange flow could fully flush a band of vegetation extending $O(100\,\mathrm{m})$ from the shore. For many field situations, this is equivalent to a complete drainage of the water within the canopy. The cold water leaving the canopy travels between 430 to 520 m into the open water. This example shows the significance of the exchange flow between canopy and open water during a diurnal cycle and the need to consider the resulting effects in modelling flow and transport in vegetated regions.

This material is based on work supported by the US National Science Foundation under grant EAR0509658. Any opinions, findings or recommendations expressed herein are those of the authors and do not necessarily reflect the views of the USNSF. The first author would like to acknowledge the financial support received from Sharif University of Technology during his sabbatical stay at Massachusetts Institute of Technology.

REFERENCES

Adams, E. E. & Wells, S. A. 1984 Field measurements on side arms of Lake Anna, VA. *J. Hydraul. Engng* **110** (6), 773–793.

Bowmaker, A. P. 1976 The physico-chemical limnology of the Mwenda River mouth, Lake Kariba. *Arch. Hydrobiol.* **77**, 66–108.

Chimney, M. J., Wenkert, L. & Pietro, K. C. 2006 Patterns of vertical stratification in a subtropical constructed wetland in south Florida (USA). *Ecol. Engng* **27**, 322–330.

Coates, M. & Patterson, J. 1993 Unsteady natural convection in a cavity with non-uniform absorption of radiation. *J. Fluid Mech.* **256**, 133–161.

Coates, M. & Patterson, J. 1994 Numerical simulations of natural convection in a cavity with nonuniform internal sources. *Intl J. Heat Fluid Flow* **15**(3), 218–225.

Dale, H. & Gillespie, T. 1976 The influence of floating vascular plants on the diurnal fluctuations of temperature near the water surface in early spring. *Hydrobiol.* **49**, 245–256.

Farrow, D. & Patterson, J. 1993 On the response of a reservoir sidearm to diurnal heating and cooling. *J. Fluid Mech.* **246**, 143–161.

Farrow, D. & Patterson, J. 1994 The daytime circulation and temperature structure in a reservoir sidearm. *Intl J. Heat Mass Transfer* **37**(13), 1957–1968.

Furukawa, K., Wolanski, E. & Mueller, H. 1997 Currents and sediment transport in mangrove forests. *Estuary. Coast. Shelf Sci.* **44**, 301–310.

Horsch, G., Stefan, H. & Gavali, S. 1994 Numerical simulation of cooling-induced convective currents on a littoral slope. *Intl J. Numer. Meth. Fluids* **19**, 105–134.

James, W. & Barko, J. 1991*a* Estimation of phosphorous exchange between littoral and pelagic zones during nighttime convective circulation. *Limnol. Ocean.* **36**(1), 179–187.

James, W. & Barko, J. 1991*b* Littoral-pelagic phosphorus dynamics during nighttime convective circulation. *Limnol. Ocean.* **36**(5), 949–960.

James, W., Barko, J. & Eakin, H. 1994 Convective water exchanges during differential cooling and heating: implications for dissolved constituent transport. *Hydrobiologia* **294**(2), 167–176.

Kadlec, R. H. 1990 Overland flow in wetlands: Vegetation resistance. *J. Hydraul. Engng* **116**(5), 691–706.

Kalff, J. 2002 *Limnology: Inland Water Ecosystems*. Prentice-Hall.

Lei, C. & Patterson, J. C. 2002 Natural convection in a reservoir sidearm subject to solar radiation: experimental observations. *Exps. Fluids* **32**(5), 590–599.

Lei, C. & Patterson, J. C. 2003 A direct three-dimensional simulation of radiation-induced natural convection in a shallow wedge. *Intl J. Heat Mass Transfer* **46**, 1183–1197.

Leonard, B. P. 1991 The ULTIMATE conservative difference scheme applied to unsteady one–dimensional advection. *Computer Meth. Appl. Mech. Engng* **88**,17–74.

Leonard, L. & Luther, M. 1995 Flow hydrodynamics in tidal marsh canopies. *Limnol. Oceanogr*, **40**, 1474–1484.

MacIntyre, S., Romero, J. R. & Kling, G. W. 2002 Spatial-temporal variability in surface layer deepening and lateral advection in an embayment of Lake Victoria, East Africa. *Limnol. Oceanogr*, **47**(3), 656–671.

MacIntyre, S. & Melack, J. 1995 Vertical and Horizontal transport in lakes: linking littoral, benthic and pelagic habitats. *J. N. Am. Benthol. Soc*. **14**, 599–615.

Mazda, Y., Wolanksi, E., King, B., Sase, A., Ohtsuka, D. & Magi, M. 1997 Drag forces due to vegetation in mangrove swamps. *Mangr. Salt Marsh* **1**, 193–199.

Monismith, S., Imberger J. & Morison, M. 1990 Convective motions in the sidearm of a small reservoir. *Limnol. Oceanogr*, **35**(8), 1676–1702 .

Nepf, H. & Oldham, C. 1997 Exchange dynamics of a shallow contaminated wetland. *Aquatic Sci.* **59**(3), 193–213.

Oldham, C. & Sturman, J. 2001 The effect of emergent vegetation on convective flushing in shallow wetlands: Scaling and experiments. *Limnol. Oceanogr*, **46**(6), 1486–1493.

Roget, E. & Colomer, J. 1996 Flow characteristics of a gravity current induced by differential cooling in a small lake. *Aquat. Sci.* **58**(4), 367–377.

Roget, E., Colomer, J., Casamitjana, X. & Llebot, J. E. 1993 Bottom currents induced by baroclinic forcing in Lake Banyoles (Spain). *Aquat. Sci.* **55**(3), 206–227.

Sartoris, J. J., Thullen, J. S., Barber, L. B. & Salas, D. E. 2000 Investigation of nitrogen transformations in a southern California constructed wastewater treatment wetland. *Ecol. Eng*ng **14**, 49–65.

Shin, J. O., Dalziel, S. B. & Linden, P. F. 2004 Gravity currents produced by lock exchange. *J. Fluid Mech.* **521**, 1–34.

Sturman, J. J. & Ivey, G. N. 1998 Unsteady convective exchange flows in cavities. *J. Fluid Mech.* **368**, 127–153.

Sturman, J. J., Oldham, C. E. & Ivey, G. N. 1999 Steady convective exchange flows down slopes. *Aquat. Sci.* **61**, 260–278.

Tanino, Y. & Nepf, H. 2008 Laboratory investigation of mean drag in a random array of rigid, emergent cylinders. *J. Hydraul. Engng ASCE* **134**, 34–41.

Tanino, Y., Nepf, H. & Kulis, P. S. 2005 Gravity currents in aquatic canopies. *Water Resour. Res.* **41**, W12402, doi:10.1029/2005WR004216.

Ultsch, G. 1973. The effect of water hyacinth (Eichhornia crassipes) on the microenvironment of aquatic communities. *Archiv. Hydrobiologia* **72**, 460–473.

Valiela, I, Teal, J. & Deuser, W. 1978 The nature of growth forms in the salt marsh grass *Spartina alterniflora*. *Am. Nat*. **112**, 461–470.

White, F. M. 1991 *Viscous Fluid Flow*. McGraw-Hill.

Zhang, X. & Nepf, H. 2008 Density-driven exchange flow between open water and aquatic canopy. *Water Resour. Res.* (submitted).

Zohary, T. & Madeira, A. 1990 Structural, physical and chemical characteristics of *Microcystis aeruginosa* hyperscum from a hypertrophic lake. *Fresh Water Biol.* **23**, 339–352.